Supplementary Materials

HEAT LOSSES IN APPLIED SMOULDERING SYSTEMS: SENSITIVITY ANALYSIS VIA ANALYTICAL MODELLING

Tarek L. Rashwan [a, b], José L. Torero [c], Jason I. Gerhard [a*]

[a] Department of Civil and Environmental Engineering, The University of Western Ontario, London, Ontario N6A 5B9, Canada

[b] Department of Civil Engineering, Lassonde School of Engineering, York University, Toronto, Ontario, M3J 1P3, Canada [1]

[c] Department of Civil, Environmental and Geomatic Engineering, University College London, London, WC1E 6BT, UK

* Corresponding author at: Department of Civil and Environmental Engineering, The University of Western Ontario, Spencer Engineering Building, Rm. 3029, London, Ontario N6A 5B9, Canada. Tel.: +1 (519) 661 4154; fax: +1 (519) 661 3942. E-mail address: jgerhard@uwo.ca (J. I. Gerhard).

[1] Present address.

S1. Discussion on Eq. (1)

Equation (1) can be integrated over time to describe the overall energy accumulated in a smouldering system (i.e., $E_{net}(t) = \int \dot{E}_{net}(t)dt$). The $E_{net}(t)$ profile and evolution of other energy terms from Eq. (1) are instructive in understanding multiple aspects common to many applied smouldering systems. In Fig. S1, the evolution of Eq. (1) throughout propagation is visualized from modelling two forward smouldering systems that are reaction-leading: (*i*) a laboratory-sized system with a 0.35 m fuel bed length (Run #2 in Fig. S1) and (*ii*) a much longer system with a 2.8 m fuel bed length (Run #4 in Fig. S1). The Dimensionless Time (DT) was defined in Fig. S1 following the method in [1]. See [2] for further details on these simulations.

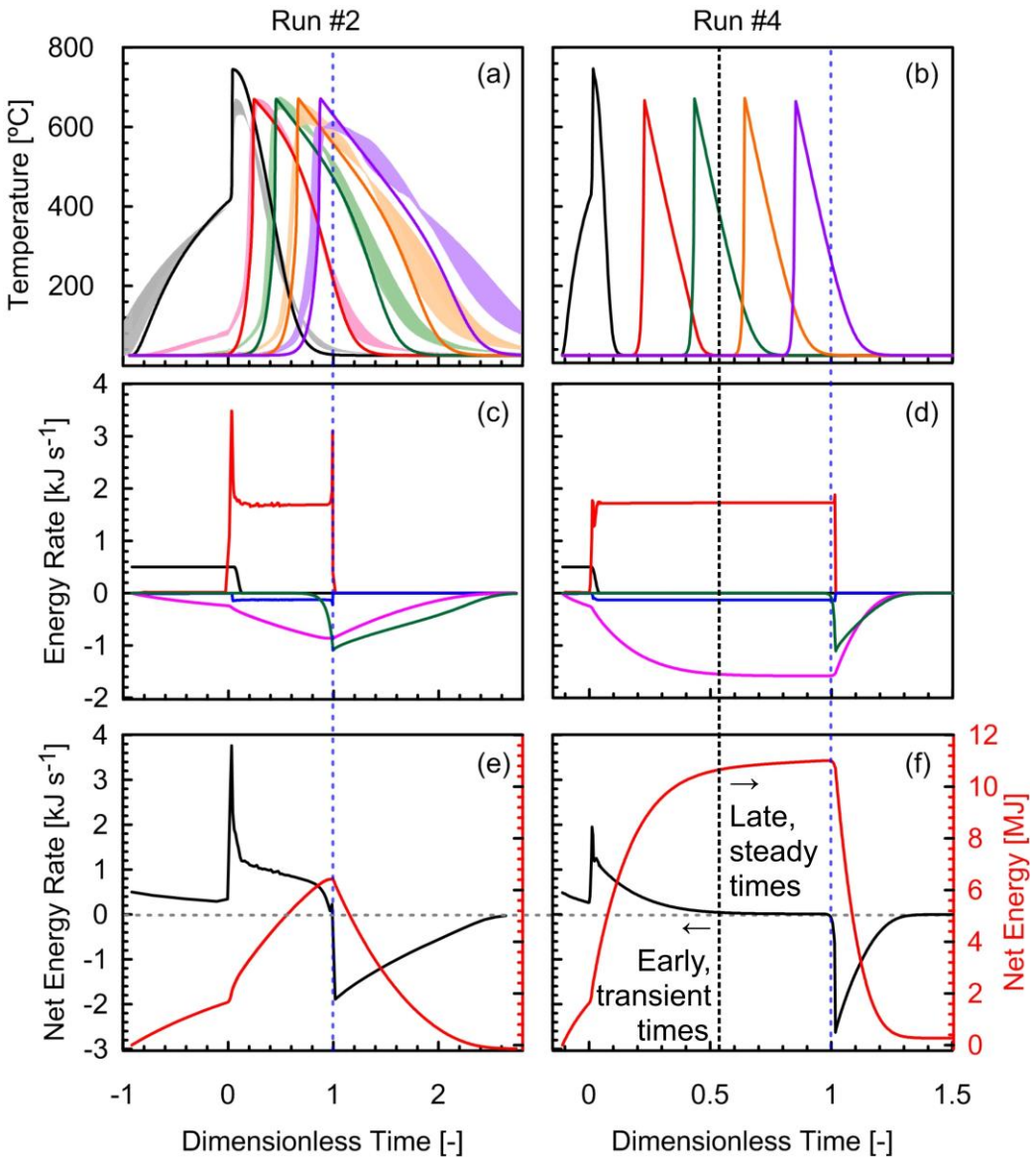

Fig. S1. One-dimensional numerical simulations from [2] showing: (a–b) solid lines indicate temperatures from smouldering bitumen embedded within sand versus Dimensionless Time (DT), where the shaded lines in (a) show experimental results from three repeats reactor [3]. DT = 0 corresponds to ignition and DT = 1 corresponds to the end of propagation (i.e., when the smouldering front reached the end of the fuel bed, noted in (a-f) with a dashed blue vertical line). Colours describe: (a) thermocouple positions from 0.12 (black) to 0.40 m (purple) with 0.07 m intervals; (b) 0.12 (black) to 2.92 m (purple) with 0.70 m intervals; (c–d) energy rate for each component in Eq. (1) versus DT (i.e., $\dot{E}_{in}(t)$ (black), $\dot{E}_{oxid}(t)$ (red), $\dot{E}_{pyr}(t)$ (blue), $\dot{E}_{loss}(t)$ (magenta), and $\dot{E}_{out}(t)$ (green)); and (e–f) $\dot{E}_{net}(t)$ (black) and $E_{net}(t)$ (red) versus DT, where the dashed horizontal grey line marks $\dot{E}_{net}$ = 0 and the dashed vertical black line in (f) shows when $\dot{E}_{loss}(t) = 0.9\dot{E}_{oxid}(t)$ (when the front propagated ~1.6 m), thereby delineating the early, transient times from late, steady times (adapted from [2]).

The $\dot{E}_{net}(t)$ and $E_{net}(t)$ profiles in Fig. S1 are governed by the evolution of $\dot{E}_{oxid}(t)$ and $\dot{E}_{loss}(t)$. Furthermore, $\dot{E}_{oxid}(t)$ is roughly constant throughout time, which aligns with many other applied smouldering studies (e.g., [2, 4-7]). However, $\dot{E}_{loss}(t)$ is not steady and increases with time. As the systems modelled in Fig. S1 are reaction-leading (i.e., $v_{oxid} > v_{cool}$ [8]), perimeter heat losses draw from the lengthening cooling zone, which exposes an increasingly longer heated region to losses. As shown in the $\dot{E}_{loss}(t)$ (Fig. S1(d)) and $E_{net}(t)$ and $\dot{E}_{net}(t)$ (Fig. S1(f)) profiles, these losses eventually plateau as $\dot{E}_{loss}(t)$ approaches the same magnitude as $\dot{E}_{oxid}(t)$. This interplay between $\dot{E}_{loss}(t)$ and $\dot{E}_{oxid}(t)$ may be separated into two temporal regions, here delineated for discussion when $\dot{E}_{loss}(t)$ = 0.9$\dot{E}_{oxid}(t)$ in Run #4 (Fig. S1(f)): (*i*) the *early, transient times:* when a decreasing fraction of the energy released from oxidation accumulates in the smouldering system $\left(\dot{E}_{loss}(t) < \dot{E}_{oxid}(t)\right)$ and (*ii*) the *late, steady times:* when the rate of heat losses nearly balances the rate of energy released from smouldering $\left(\dot{E}_{loss}(t) \sim \dot{E}_{oxid}(t)\right)$. At these late times, most of the energy generated from smouldering is lost as heat losses, therefore, the final cooling zone length $(l_{cool,f})$ from Fig. 1 becomes approximately steady at a maximum value. As shown in Run #4 in Fig. S1, the late-time condition is approximated after the front propagated ~1.6 m and the smouldering behaviour in Run #2 all occurred within the early times, as the total simulated fuel bed length was only 0.35 m. An approximation of the $l_{cool,f}$ based on the condition $\dot{E}_{loss}(t) = \dot{E}_{oxid}(t)$ is presented below in Section S4.

S2. Discussing the use of Eq. (4)

The h_{sg} correlation in Eq. (4) is different than in Kuznetsov [9], who approximated the effect of local thermal non-equilibrium (LTNE) using a correlation from Dixon and Cresswell [10]. The correlation from [10], along with other widely used correlations (e.g., [11]), overestimates the heat transferred between gas and solid phases at low Reynold's numbers relevant for applied smouldering combustion ($1 \leq Re \leq 40$) [3, 12]. By contrasting numerical and experimental results, Zanoni et al., [3] showed that predicted temperatures were considerably more accurate with the new h_{sg} correlation from [12] than compared to the widely used correlation from [11]. Choosing an alternative h_{sg} correlation was approached carefully here because a large temperature difference between phases precludes a perturbation analysis [9, 13, 14]. However, the numerical results from [3] showed that the temperature difference between phases, which is large near the reaction and inert heating zones (30-70% of $T_{peak} - T_{amb}$), is sufficiently low upstream of smouldering in the cooling zone (<10% of $T_{peak} - T_{amb}$). The large temperature difference between phases in the reaction and inert heating zones is due to the exothermic degradation on the surface of the fuel [15] and may be too large to permit a perturbation analysis (though it may be permissible under some conditions, e.g., [16]). However, because the degree of LTNE is dampened upstream of the smouldering front in the region under interest here, the temperature difference between phases was assumed sufficiently small to follow the same perturbation method as Kuznetsov [9].

S3. Summarizing the Dimensionless form of Eqs. (2-3)

By using the descriptions for dimensionless time, distances, temperatures, and difference between phase temperatures, Eqs. (2-3) become [9]:

$$\frac{\partial \theta_g}{\partial \tau} + \frac{\partial \theta_g}{\partial \xi_x} = \frac{\partial^2 \theta_g}{\partial {\xi_x}^2} + \frac{\partial^2 \theta_g}{\partial {\xi_r}^2} + \frac{1}{\xi_r}\frac{\partial \theta_g}{\partial \xi_r} + O(\delta) \tag{S.1}$$

$$\Delta\theta = \frac{\partial \theta_g}{\partial \tau} + \Lambda_1 \frac{\partial \theta_g}{\partial \xi_x} - \Lambda_2 \left[\frac{\partial^2 \theta_g}{\partial {\xi_x}^2} + \frac{\partial^2 \theta_g}{\partial {\xi_r}^2} + \frac{1}{\xi_r}\frac{\partial \theta_g}{\partial \xi_r}\right] \tag{S.2}$$

In dimensionless form, the initial and boundary conditions are [9]:

$$\theta_g(\xi_x, \xi_r, 0) = 0 \tag{S.3}$$

$$\theta_g(0, \xi_r, \tau) = 1 \tag{S.4}$$

$$\frac{\partial \theta_g}{\partial \xi_r}(\xi_x, R, \tau) = \alpha\left(1 - \theta_g(\xi_x, R, \tau)\right) \tag{S.5}$$

$$\frac{\partial \theta_g}{\partial \xi_x}(L(\tau), \xi_r, \tau) = 0 \tag{S.6}$$

Additional insight into the relevant mathematics for the solutions in Eq. (10) can be found in [17-19].

S4. Approximating the Steady Cooling Zone Length at Late-Time Conditions

An approximate steady, maximum cooling zone length $\left(l_{cool,f}\right)$ trailing behind the smouldering front was estimated at late-time conditions, which was defined in the Introduction, when the rate of energy generated from smouldering, $\dot{E}_{oxid}$, balance the rate of losses behind the smouldering front, $\dot{E}_{loss}$:

$$\dot{E}_{oxid} = \iiint_V \Delta H_{oxid} \cdot W \, dV \tag{S.7}$$

$$\dot{E}_{loss} = \iiint_V \frac{1}{r}\frac{\partial}{\partial r}\left(k_{bulk} r \frac{\partial T}{\partial r}(r, x)\right) dV \tag{S.8}$$

Here, ΔH_{oxid} is the heat of smouldering, $W = d\dot{m}''_{fuel}/dx$ is the volumetric mass loss rate (which assumes smouldering propagation is fuel-limited, a typical assumption when smouldering fuel within inert media as virtually all fuel is consumed within the thin reaction zone [6, 20-25]), $\dot{m}''_{fuel}$ is the mass flux of fuel consumed, and k_{bulk} is the effective bulk conductivity (see Methodology, Section 2.2 for additional details). This is a similar type of analysis recently performed by Lin and Huang [26] to determine the minimum reactor diameter that would support self-sustained smouldering of peat (which facilitated a much thicker reaction zone than most applied smouldering systems that use fuel imbedded within inert porous media [25]). If all properties in Eqs. (S.7-S.8) are assumed steady at late-times (as discussed in the Introduction and identified in Fig. S1) and assuming effectively all heat losses draw from the cooling zone [6] then, by integrating over the reactor volume, $\dot{E}_{oxid}$ and $\dot{E}_{loss}$ can be simplified as:

$$\dot{E}_{oxid} = \pi r_o^2 \Delta H_{oxid} v_{oxid} (1-\phi)\rho_s \left(m_{fuel}/m_s\right) \tag{S.9}$$

$$\dot{E}_{loss} = 2\pi r_o k_{bulk} \int_0^{l_{cool,f}} \frac{\partial T}{\partial r}(x, r_0)dx \tag{S.10}$$

r_o is the reactor outer radius, v_{oxid} is the smoulder velocity, and $(1-\phi)\rho_s\left(m_{fuel}/m_s\right)$ is the bulk density of fuel in the fuel/sand mixture, where the mass fraction of fuel to sand is m_{fuel}/m_s. Using the radial boundary condition in Eq. (7) and assuming the average driving temperature difference across the cooling zone can be approximated as $\left(T_{peak} - T_{amb}\right)/2$, where T_{peak} and T_{amb} are the peak smouldering and ambient temperatures, respectively, an order-of-magnitude estimate of $l_{cool,f}$ can be described:

$$l_{cool,f} \sim \frac{\Delta H_{oxid} v_{oxid} (1-\phi) \rho_s \left(\frac{m_{fuel}}{m_s}\right) r_o \left(\frac{x_c}{\alpha} + r_o\right)}{k_{bulk}\left(T_{peak} - T_{amb}\right)} \quad \text{(S.11)}$$

In addition to the relevant smouldering properties summarized in Table 1, the other parameters relevant for Eq. (S.11) from smouldering granular activated carbon are: $(1-\phi)\rho_s\left(m_{fuel}/m_s\right)$ = 39 kg m^{-3} and ΔH_{oxid} = 25 MJ kg^{-1}. Further details on experiments with these smouldering properties can be found in [5]. Here, the change in radius thickness due to insulation is assumed small so that the outer radius remains ~r_o, x_c is the characteristic heat transfer length, and α is the non-dimensional modified heat transfer coefficient (see the Methodology, Section 2.2 for details). Here, r_o is taken as the characteristic heat transfer length across the reactor, therefore $(x_c/\alpha + r_o)/k_{bulk}$ is used to approximate the thermal resistance out of the reactor from the outer insulation and porous media.

Equation (S.11) represents a simplified, order-of-magnitude estimate of the steady $l_{cool,f}$ by assuming it is controlled by heat diffusing across the radial boundary condition out of an insulated reactor. Figure S2 shows that $l_{cool,f}$ is highly sensitive to the reactor radius and sensitive to the insulation quality at small radii (approximately at $r_o < O$(0.1 m)). Furthermore, regardless of insulation, reactors with radii $r_o < O$(0.01 m) have a $l_{cool,f} < O$(0.1 m) and reactors with radii $r_o > O$(0.1 m) have a $l_{cool,f} > O$(1.0 m). Because of the boundary condition used in Eq. (8), the results from the transient analysis using Eqs. (10-11) are most valuable when smouldering propagation is far from the late-time, steady-state conditions, i.e., during the early, transient times (identified from Fig. S1 and discussed in the Introduction). At these early times, the cooling length is shorter than the

approximated maximum, steady cooling zone length, $l_{cool}(t) < l_{cool,f}$. As discussed in the Introduction and highlighted in Fig. 1, $l_{cool}(t)$ is approximately bounded by v_{oxid} and the trailing cooling velocity, v_{cool}. However, as shown in Fig. 1, the end of the cooling zone extends behind the cooling front because of conduction and grows with $\sqrt{t}/2$ [8, 27]. Therefore, a conservatively long estimate of the cooling length at the end of propagation, $l_{cool}(t_f)$, can be approximated by assuming the whole distance from the smouldering front to the column inlet roughly represents $l_{cool}(t_f)$:

$$l_{cool}(t_f) \sim l(t_f) \tag{S.12}$$

$l(t_f)$ is the final domain length at the end of propagation (discussed in the Methodology, Section 2.1) and t is the cooling time. Therefore, the maximum $l_{cool}(t_f)$ modelled (at t_f = 45 min) using Eq. (S.12) is 0.33 m, so the results with reactor radii > O(0.1 m) are most valuable because they represent estimates that are very far from the steady, late-times. Since the primary goal here is to draw implications for commercial batch systems (i.e., > 0.1 m radii, e.g., [28-32]), these large radii results are highly relevant. However, the estimates for reactors with small radii still show a key trend in heat losses, though there is greater error due to an incomplete description of the problem. Therefore, the results with reactor radii ≤ O(0.01 m) in Fig. 5 are presented to qualitatively show the diminishing role of heat losses as the reactor radius increases towards commercial scale systems.

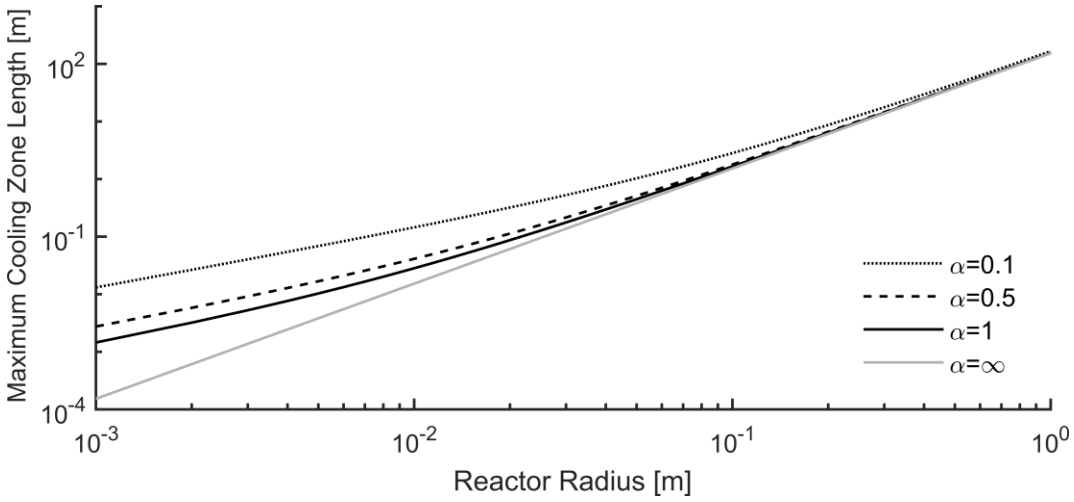

Fig. S2. Showing the approximate relationship between reactor radius and steady cooling zone length using Eq. (S.11) using the values from Table 1 and assuming no insulation ($\alpha = \infty$), or the insulation was relatively poor ($\alpha = 1$), good ($\alpha = 0.5$), and very good ($\alpha = 0.1$).

In addition, the $l_{cool,f}$ from studies used in Figs. S1 and 5 were approximated assuming the columns had no insulation (i.e., $\alpha = \infty$) to estimate a conservatively short $l_{cool,f}$. These $l_{cool,f}$ estimates were divided by their respective $l(t_f)$ at the end of propagation to estimate a conservatively long $l_{cool}(t_f)$ from Eq. (S.12). The properties from these studies are summarized in Table S1 and the results are plotted in Fig. S3. Nearly all studies used similar coarse sand as in [5], so the properties measured by [12] were used to estimated the air and sand thermophysical parameters over each experiment's T_{peak} to T_{amb} (where T_{amb} was assumed to be 294 K in all cases). However, [22] simulated carbon embedded within alumina particles from [20], so the reported effective alumina parameters were used instead. Furthermore, the method from [33] was used to estimate the ΔH_{oxid} from [22] using the reported fr_{CO} = 0.314 released from oxidizing carbon, and the ΔH_{oxid} from [2, 6] was corrected for the effect of simulated pyrolysis reported in [6].

The experimental errors from Rashwan et al., [5] are included in Table S1, where the error in ΔH_{oxid} is driven by the errors in the fr_{CO} measurements. These errors match with common errors reported from similar applied smouldering studies (e.g., [1, 3, 34-37]). The coarse sand properties were used from careful measurements in [12], who showed the $C_{p_s}(T)$ and $k_s(T)$ both exhibited a measurement error of 5% and the functions used to approximate the $C_{p_g}(T)$ and $k_g(T)$ varied from the tabulated values in Bergman et al., [38] by ≤ 1%. The sand and air property errors are further discussed in [12].

Altogether, Fig. S3 shows that most of the experimental data used in Fig. 5 exhibited $l(t_f)/l_{cool,f}(\alpha = \infty) < 1$, a highly conservative condition. Furthermore, the two data points from [2] show simulated smouldering systems progressed much closer to the late-time, steady-state condition (when $\dot{E}_{oxid} \sim \dot{E}_{loss}$) by increasing the propagation length from 0.35 m (in Run #2) to 2.8 m (in Run #4). This aligns with the discussion above in Section S1. However, though the data from [21, 22] both show the $l(t_f)/l_{cool,f}(\alpha = \infty) > 1$, these studies used [21] and modelled [22] smouldering systems that were quite well insulated. Therefore, their $l_{cool,f}$ may be better predicted between the two the top curves in Fig. S3 (i.e., between $l_{cool,f}(\alpha = 0.5)$ and $l_{cool,f}(\alpha = 0.1)$, as it also aligns with their positions in Fig. 5), which both data points are reasonably below. Most importantly, the key experimental data from [5] show $l(t_f)/l_{cool,f}(\alpha = \infty) < 1$. These data points are the most critical comparisons and provide the most confidence in Fig. 5 (see Results and Discussion).

Table S1.
Input Parameters for Fig. S3.

Par.	Ref. [5]	Ref. [5]	Ref. [21]	Ref. [22]	Ref. [6]	Ref. [6]	Ref. [2]	Ref. [2]	Unit
T_{peak}	874 ± 1%	834 ± 4%	1050	740	1100	580	679	679	°C
$\rho_g u_g$	0.060 ± 3%	0.060 ± 2%	0.029	0.025	0.070	0.070	0.070	0.070	kg m^{-2} s^{-1}
v_{oxid}	8.17E-05 ± 4%	7.33E-05 ± 10%	6.67E-05	8.33E-05	1.00E-04	2.67E-05	6.93E-05	6.93E-05	m s^{-1}
$l(t_f)$	0.40	0.40	0.30	0.30	0.35	0.35	0.35	2.80	m
ϕ	0.37	0.37	0.37	0.45	0.37	0.37	0.37	0.37	-
ρ_s	2650	2650	2650	1475	2650	2650	2650	2650	kg m^{-3}
k_{bulk}	0.561	0.535	0.688	0.389	0.729	0.394	0.434	0.434	W m^{-1} K^{-1}
ΔH_{oxid}	24.9 ± 5%	24.9 ± 1%	19.5	25.4	36.0	36.0	36.0	36.0	MJ kg^{-1}
m_{fuel}/m_s	23.3 ± 0.3%	23.3 ± 2%	37.3	23.5	91.8	34.2	34.2	34.2	g kg^{-1}
r_o	0.080	0.300	0.046	0.046	0.080	0.080	0.080	0.080	m

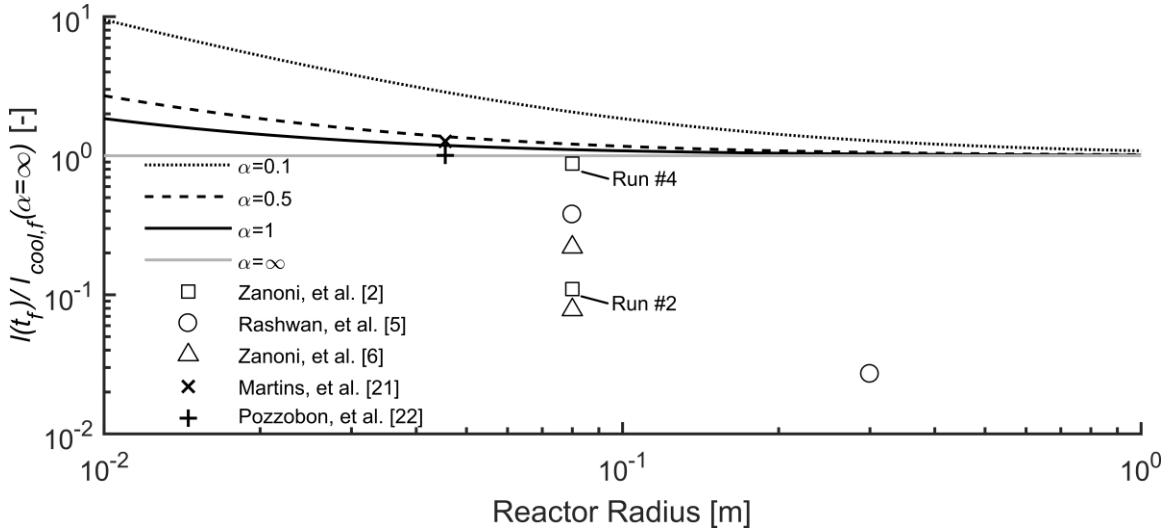

Fig. S3. Dividing the approximate final cooling zone length $l(t_f)$ by the approximate steady cooling zone length without insulation $l_{cool,f}(\alpha = \infty)$ from literature data used in Figs. S1 and 5. The lines from Fig. S2 are divided by $l_{cool,f}(\alpha = \infty)$ to illustrate the extended cooling zone lengths when accounting for insulation of various qualities. Runs #4 and #2 from [2] are labelled for further discussion.

Though the experimental/numerical data in Fig. 5 show meaningful comparisons to the model predictions, at sufficiently late times in long reactors (like shown with the simulations from [2] in Figs. S1 and S3) all system energy efficiencies in Fig. 5 would approach zero as the generation terms balance the loss terms in Eq. (1). Figure S4 illustrates this effect as all calculated system energy efficiencies (with varying reactor radius and α) decreased when the smouldering front travelled from 0.24 m to 0.33 m after 25 and 45 minutes, respectively. This balance is governed by the energy removed from heat losses and the energy generated from smouldering (seen in Fig. S1 as the late-time condition). As highlighted in Fig. S3, the system energy efficiency estimates presented from the literature in Fig. 5 appear sufficiently far from this late-time condition when the smouldering front only travelled 0.30 m in [21, 22], 0.35 m in [6], and 0.40 m in [5].

However, nearly all other parameters considered in Table 1 varied from those in [6, 21, 22]. For example, Darcy air fluxes, porous media type, fuel type and concentration all contributed to varying smouldering propagation velocities, peak temperatures (see Table S1), which all impacted the global energy balance terms summarized in Eq. (1). Therefore, the results are expected to scatter around the main trends in Fig. 5.

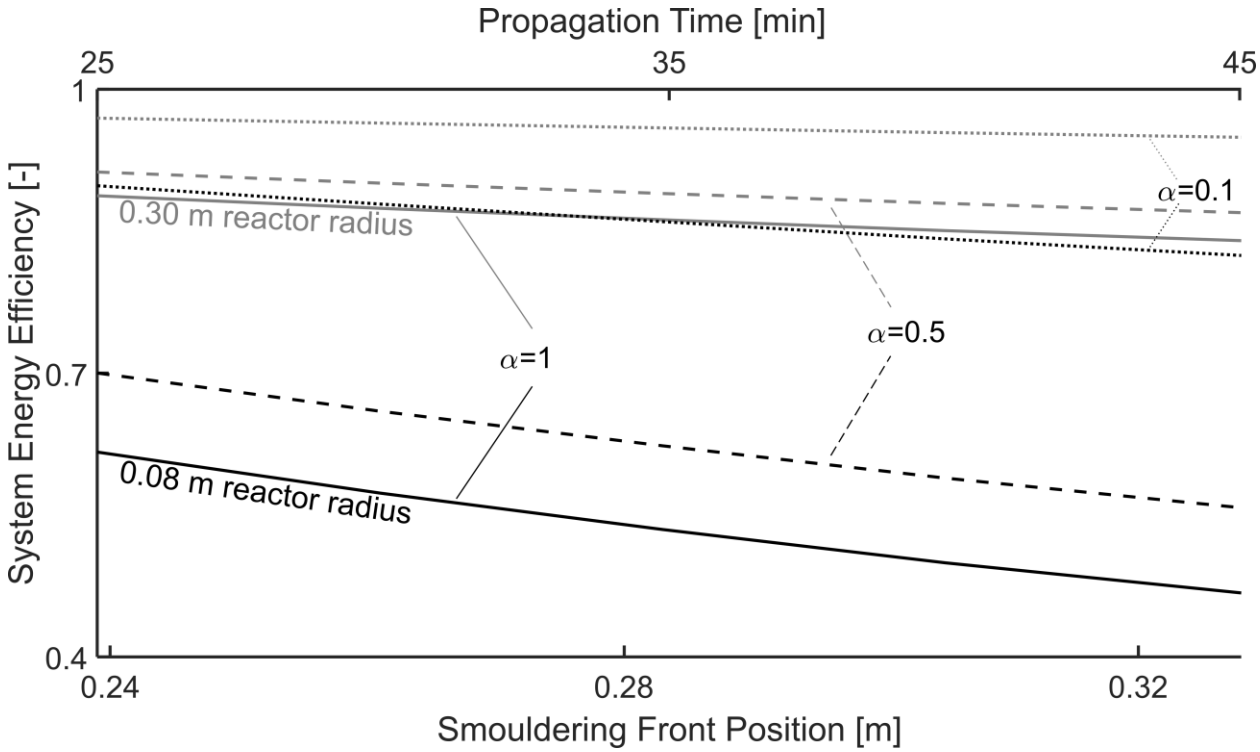

Fig. S4. System energy efficiency varying as the smouldering front progressed assuming insulation was poor ($\alpha = 1$, solid line), good ($\alpha = 0.5$, dashed line), and very good ($\alpha = 0.1$, dotted line) in a large column (0.30 m radius, grey) and small column (0.08 m radius, black).

As an alternative visualization for Fig. 5, Fig. S5 shows how the $E_{loss}(t)/E_{oxid}(t)$ (i.e., cumulative heat lost normalized to the energy released by oxidation) attenuates with increased reactor radius and decreased α. Like Fig. 5, the calculations in Fig. S5 all assumed the smouldering front travelled 0.33 m after 45 minutes. Following Eq. (14), the $E_{loss}(t)/E_{oxid}(t)$ terms were approximated as:

$1 - E_{net}(t)/E_{net,adiabatic}(t) \sim E_{loss}(t)/E_{oxid}(t)$.

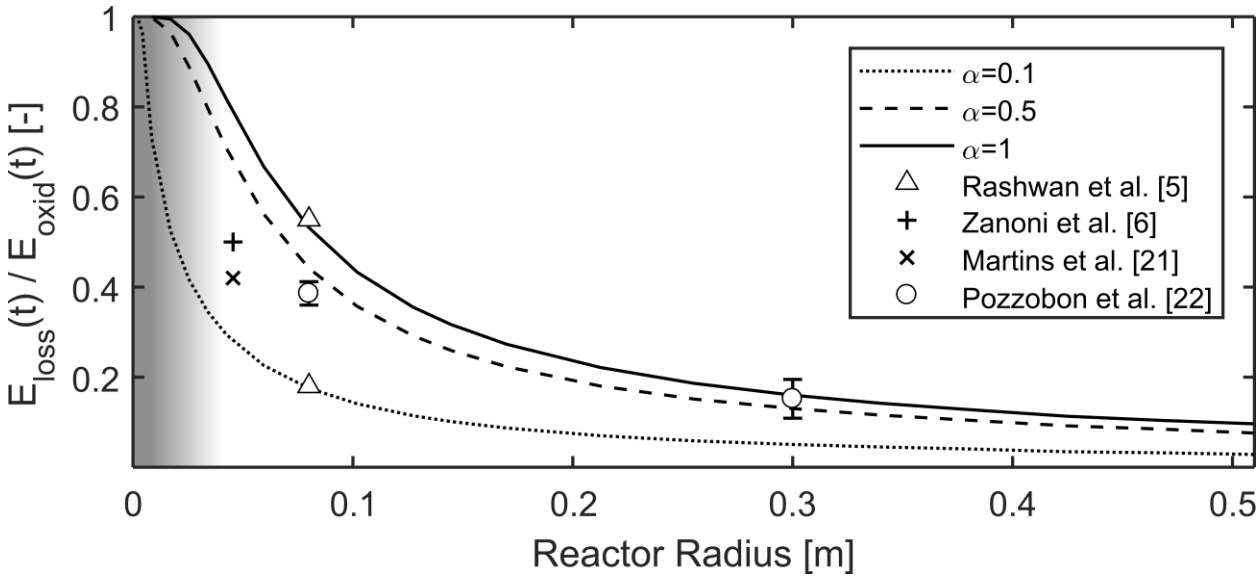

Fig. S5. $E_{loss}(t)/E_{oxid}(t)$ values estimated when the smouldering front travelled 0.33 m after 45 minutes of cooling in reactors with varying radii and assuming insulation was relatively poor ($\alpha = 1$), good ($\alpha = 0.5$), and very good ($\alpha = 0.1$). Experimental and numerical observations from similar studies are plotted for comparison. The error bars on experimental values represent the median absolute deviations of estimates. The gradient gray area approximately shows the region where the assumptions regarding the boundary condition in Eq. (8) becomes less valid as the radius decreases to O(0.01 m).

Though the insulation quality was varied in Fig. 5 to capture the envelope in system energy efficiencies reported in the literature, this does not imply that the differences in the data compared in Fig. 5 was solely due to varying the insulation quality. In fact, all comparisons presented in Fig. 5 used (or assumed) similar insulation qualities (detailed

below). As mentioned above and discussed in the Results and Discussions, the effects of all energy generation and loss terms affect the net stored energy in Eq. (1) that lead to the varying system energy efficiencies observed in Fig. 5. As seen in the parameters in Table S1, all studies compared in Fig. 5 used a range of smouldering conditions that led to the observed system energy efficiencies. The insulation quality varied in Fig. 5 is one intuitive parameter that captures the envelope of results.

Regarding the insulation quality, Rashwan et al., [5] used 0.050 m thick insulation in both experiments, where the conductivities varied slightly between the 0.080 m and 0.300 m reactors, i.e., 0.034 W m^{-1} K^{-1} and 0.031 W m^{-1} K^{-1} (both at 24°C), respectively. The 1D numerical model from Zanoni et al., [2, 6] was calibrated with experiments using the same 0.080 m reactor with the same insulation used by Rashwan et al., [5]. Martins et al., [21] used two layers of similar quality insulation that were 0.003 m and 0.050 m thick and reported conductivities of 0.28 W m^{-1} K^{-1} at 982°C and 0.21 W m^{-1} K^{-1} at 1000°C, respectively. Because the insulation conductivity increases with temperature, the insulation quality used by Martins et al., [21] was probably similar to that used by Rashwan et al., [5]. Pozzobon et al., [22] calibrated a 2D numerical model to experiments performed by Baud et al., [20], who used the same experimental setup developed by Martins et al., [21] but with only the 0.050 m layer of insulation with a conductivity of 0.21 W m^{-1} K^{-1} at 1000°C. Therefore, all studies used (or assumed) a similar quality of insulation.

S5. Detailing the Integration Technique for Eq. (13)

The modelled temperatures were used to define the net stored energy density throughout the reactor using the same integration technique from [5] and summarized here:

$$\frac{E_{net}}{V}(x,r,t) = (1-\phi)\rho_s \int_{T_{amb}}^{T_s(x,r,t)} C_{p_s}(T_s)dT \tag{S.13}$$

where the sand heat capacity $\left(C_{p_s}(T) = 1.75[T] + 340.32\right)$ and sand density ($[1-\phi]\rho_s =$ 1670 kg m^{-3}) measured for coarse sand in [12] was used, as it is most commonly used in these types of smouldering experiments (e.g., [3, 5, 34, 39]). Next, a trapezoidal numerical integration method was used along the axial length of the reactor at all radial locations:

$$\frac{E_{net}}{A}(r,t) = \int_0^{l(t)} \frac{E_{net}}{V}(x,r,t)dx \tag{S.14}$$

The resulting net stored energy per unit area values, $E_{net}/A\,(r,t)$, were then summed discretely as if they represented vertical heights in a series of stacked frustums from the centre position $\left(r_{j=1} = 0\right)$ to the wall $\left(r_{j=J} = r_0\right)$:

$$E_{net}(t) = \sum_{2}^{J+1} \frac{\pi}{3}\left(\frac{E_{net}}{A}(r_{j-1},t) - \frac{E_{net}}{A}(r_j,t)\right)\left(r_j^2 + r_{j-1}^2 + r_j r_{j-1}\right) \tag{S.15}$$

A dummy value of zero net stored energy $(E_{net}/A\,(r_o, t) = 0)$ was used at the radial position at the wall $(r_{J+1} = r_o)$ to integrate the stored energy relative to the system at T_{amb}. Though Eqs. (10-11) are continuous throughout space and time, they were solved at discrete locations, where a spacing of 5% the total length was used, i.e., $\Delta\xi_r = 0.05R, \Delta\xi_x = 0.05L$. This spacing criterion resulted in ≤ 1% error in all estimates of $E_{net}(t)$. Each integration was performed using an in-house MATLAB code and took approximately one minute to perform all calculations involved in estimating one system energy efficiency value in Fig. 5, using a standard Dell Latitude E7470 laptop. Eq. (S.15) assumes the temperature distribution was axisymmetric.

S6. References

[1] L. Kinsman, J.L. Torero, J.I. Gerhard, Organic liquid mobility induced by smoldering remediation, J. Hazard. Mater., 325 (2017) 101-112.
[2] M.A.B. Zanoni, J.L. Torero, J.I. Gerhard, Determining the conditions that lead to self-sustained smouldering combustion by means of numerical modelling, Proc. Combust. Inst., 37(3) (2019) 4043-4051.
[3] M.A.B. Zanoni, J.L. Torero, J.I. Gerhard, The role of local thermal non-equilibrium in modelling smouldering combustion of organic liquids, Proc. Combust. Inst., 37(3) (2019) 3109-3117.
[4] I. Fabris, D. Cormier, J.I. Gerhard, T. Bartczak, M. Kortschot, J.L. Torero, Y.-L. Cheng, Continuous, self-sustaining smouldering destruction of simulated faeces, Fuel, 190 (2017) 58-66.
[5] T.L. Rashwan, J.L. Torero, J.I. Gerhard, The improved energy efficiency of applied smouldering systems with increasing scale, (submitted).
[6] M.A.B. Zanoni, J.L. Torero, J.I. Gerhard, Delineating and explaining the limits of self-sustained smouldering combustion, Combust. Flame, 201 (2019) 78-92.
[7] L. Yermán, R.M. Hadden, J. Carrascal, I. Fabris, D. Cormier, J.L. Torero, J.I. Gerhard, M. Krajcovic, P. Pironi, Y.-L. Cheng, Smouldering combustion as a treatment technology for faeces: Exploring the parameter space, Fuel, 147 (2015) 108-116.
[8] A.P. Aldushin, I.E. Rumanov, B.J. Matkowsky, Maximal energy accumulation in a superadiabatic filtration combustion wave, Combust. Flame, 118(1–2) (1999) 76-90.
[9] A.V. Kuznetsov, Investigation of a Non-Thermal Equilibrium Flow of an Incompressible Fluid in a Cylindrical Tube Filled with Porous Media, ZAMM-Z. Angew. Math. Me., 76(7) (1996) 411-418.
[10] A.G. Dixon, D.L. Cresswell, Theoretical prediction of effective heat transfer parameters in packed beds, AIChE J., 25(4) (1979) 663-676.

[11] N. Wakao, S. Kaguei, T. Funazkri, Effect of fluid dispersion coefficients on particle-to-fluid heat transfer coefficients in packed beds: Correlation of nusselt numbers, Chem. Eng. Sci., 34(3) (1979) 325-336.
[12] M.A.B. Zanoni, J.L. Torero, J.I. Gerhard, Determination of the interfacial heat transfer coefficient between forced air and sand at Reynold's numbers relevant to smouldering combustion, Int. J. Heat Mass Transfer, 114(Supplement C) (2017) 90-104.
[13] A.V. Kuznetsov, An investigation of a wave of temperature difference between solid and fluid phases in a porous packed bed, Int. J. Heat Mass Transfer, 37(18) (1994) 3030-3033.
[14] A.V. Kuznetsov, THERMAL NONEQUILIBRIUM FORCED CONVECTION IN POROUS MEDIA, in: D.B. Ingham, I. Pop (Eds.) Transport Phenomena in Porous Media, Pergamon, Oxford, 1998, pp. 103-129.
[15] A. Oliveira, M. Kaviany, Nonequilibrium in the transport of heat and reactants in combustion in porous media, Prog. Energ. Combust., 27(5) (2001) 523-545.
[16] C.W. Wahle, B.J. Matkowsky, A.P. Aldushin, Effects of gas-solid nonequilibrium in filtration combustion, Combust. Sci. Technol., 175(8) (2003) 1389-1499.
[17] H.S. Carslaw, J.C. Jaeger, Conduction of heat in solids, second ed., Oxford: Clarendon Press, 1959.
[18] R.W. Cleary, D.D. Adrian, Analytical Solution of the Convective-Dispersive Equation for Cation Adsorption in Soils1, Soil Sci. Soc. Am. J., 37(2) (1973) 197-199.
[19] M.T. van Genuchten, W.J. Alves, Analytical solutions of the one-dimensional convective-dispersive solute transport equation, U.S. Gov. Print. Office, Washington, DC, 1982.
[20] G. Baud, S. Salvador, G. Debenest, J.-F. Thovert, New Granular Model Medium To Investigate Smoldering Fronts Propagation—Experiments, Energ. Fuel., 29(10) (2015) 6780-6792.
[21] M.F. Martins, S. Salvador, J.F. Thovert, G. Debenest, Co-current combustion of oil shale – Part 2: Structure of the combustion front, Fuel, 89(1) (2010) 133-143.
[22] V. Pozzobon, G. Baud, S. Salvador, G. Debenest, Darcy Scale Modeling of Smoldering: Impact of Heat Loss, Combust. Sci. Technol., 189(2) (2017) 340-365.
[23] P. Pironi, Smouldering combustion of liquids in porous media for remediating NAPL-contaminated soils, PhD, The University of Edinburgh, Edinburgh, UK, 2009.
[24] P. Pironi, C. Switzer, J.I. Gerhard, G. Rein, J.L. Torero, Self-sustaining smoldering combustion for NAPL remediation: laboratory evaluation of process sensitivity to key parameters, Environ. Sci. Technol., 45(7) (2011) 2980-2986.
[25] J.L. Torero, J.I. Gerhard, M.F. Martins, M.A.B. Zanoni, T.L. Rashwan, J.K. Brown, Processes defining smouldering combustion: Integrated review and synthesis, Prog. Energ. Combust., 81 (2020) 100869.
[26] S. Lin, X. Huang, Quenching of smoldering: Effect of wall cooling on extinction, Proc. Combust. Inst., (2020) https://doi.org/10.1016/j.proci.2020.1005.1017.
[27] J. Bruining, A.A. Mailybaev, D. Marchesin, Filtration Combustion in Wet Porous Medium, SIAM Journal on Applied Mathematics, 70(4) (2009) 1157-1177.
[28] R. Solinger, G.P. Grant, G.C. Scholes, C. Murray, J.I. Gerhard, STARx Hottpad for smoldering treatment of waste oil sludge: Proof of concept and sensitivity to key design parameters, Waste Manage. Res., 38(5) (2020) 554-566.

[29] G. Sabadell, G. Scholes, D. Thomas, C. Murray, P. Bireta, G. Grant, D. Major, Ex situ treatment of organic wastes or oil-impacted soil using a smoldering process, WIT Trans. Ecol. Environ., 231 (2019) 367-376.
[30] G. Sabadell, D. Thomas, P. Bireta, G. Scholes, C. Murray, B. Boulay, G. Grant, D. Major, Treatment of Oil-Impacted Soil and Oily Waste: Overview of Two Field Demonstration Projects, in: SPE International Conference and Exhibition on Health, Safety, Security, Environment, and Social Responsibility, Society of Petroleum Engineers, Abu Dhabi, UAE, 2018, pp. SPE-190566-MS.
[31] J.I. Gerhard, G.P. Grant, J.L. Torero, Chapter 9 - Star: a uniquely sustainable in situ and ex situ remediation process, in: D. Hou (Ed.) Sustainable Remediation of Contaminated Soil and Groundwater, Butterworth-Heinemann, 2020, pp. 221-246.
[32] D. Thomas, P. Bireta, K. McVey, D. Segal, M. Hudson, B.-H. Sami, S. Gabriel, A Novel, Cost Effective and Easily Scaled Solution for On-Site Treatment of Oily Wastes, in: International Petroleum Technology Conference, International Petroleum Technology Conference, Dhahran, Kingdom of Saudi Arabia, 2020, pp. IPTC-19951-MS.
[33] M.F. Martins, S. Salvador, J.F. Thovert, G. Debenest, Co-current combustion of oil shale – Part 1: Characterization of the solid and gaseous products, Fuel, 89(1) (2010) 144-151.
[34] T.L. Rashwan, J.I. Gerhard, G.P. Grant, Application of self-sustaining smouldering combustion for the destruction of wastewater biosolids, Waste Manage., 50 (2016) 201-212.
[35] M. Salman, J.I. Gerhard, D.W. Major, P. Pironi, R. Hadden, Remediation of trichloroethylene-contaminated soils by star technology using vegetable oil smoldering, J. Hazard. Mater., 285 (2015) 346-355.
[36] J. Wang, G.P. Grant, J.I. Gerhard, The influence of porous media heterogeneity on smouldering remediation, J. Contam. Hydrol., 237 (2021) 103756.
[37] A.L. Duchesne, J.K. Brown, D.J. Patch, D. Major, K.P. Weber, J.I. Gerhard, Remediation of PFAS-Contaminated Soil and Granular Activated Carbon by Smoldering Combustion, Environ. Sci. Technol., 54(19) (2020) 12631-12640.
[38] T.L. Bergman, A.S. Lavine, F.P. Incropera, D.P. DeWitt, Fundamentals of Heat and Mass Transfer, seventh ed., John Wiley & Sons, New York, NY, 2011.
[39] P. Pironi, C. Switzer, G. Rein, A. Fuentes, J.I. Gerhard, J.L. Torero, Small-scale forward smouldering experiments for remediation of coal tar in inert media, Proc. Combust. Inst., 32(2) (2009) 1957-1964.